Electronic Supplementary Material (ESI) for Nanoscale.


# Supporting Information: Dislocation driven spiral and non-spiral growth in layered chalcogenides: morphology, mechanism, and mitigation

Yifan Nie,[†] Adam T. Barton,[†] Rafik Addou,[†] Yongping Zheng,[†] Lee A. Walsh,[†] Sarah M. Eichfeld,[‡] Ruoyu Yue,[†] Christopher Cormier,[†] Chenxi Zhang,[†] Qingxiao Wang,[†] Chaoping Liang,[†] Joshua A. Robinson,[‡] Moon Kim,[†] William Vandenberghe,[†] Luigi Colombo,[§] Pil-Ryung Cha,[‖] Robert M. Wallace,[†] Christopher L. Hinkle,[†] and Kyeongjae Cho[*,†]

†*Department of Materials Science and Engineering, The University of Texas at Dallas, Richardson, Texas 75080, United States*

‡*Department of Materials Science and Engineering, The Pennsylvania State University, University Park, Pennsylvania 16802, United States*

¶*Center for Two-Dimensional and Layered Materials, The Pennsylvania State University, University Park, Pennsylvania 16802, United States*

§*Texas Instruments Incorporated, 13121 TI Boulevard, Dallas, Texas 75243, United States*

‖*School of Advanced Materials, Kookmin University, Jeongneung-gil 77, Seongbuk-gu, Seoul, 136-702, Korea*

E-mail: kjcho@utdallas.edu

Phone: +1 (972)883 2845

# The phase field method

## Derivation and justification of the governing equations

The derivation below follows the classic references on the phase-field method.[1–4] The Ginzburg-Landau free energy equation uses the spatial distribution of a continuous order parameter (the phase field $\psi$) to determine the energy of the system:[1]

$$H[\psi, T] = \int_V \{\frac{1}{2}|W\nabla\psi|^2 + f[\psi(\overrightarrow{x}), T(\overrightarrow{x})]\}d^3x, \tag{S1}$$

In which the first term of the integrand corresponds to the interface energy, with $W$ being the interface width, and the second term is the bulk free energy density, as a function of the local phase and temperature. In this work, a two-dimensional isothermal system is considered. Dropping the temperature field ($T(\overrightarrow{x})$) and rewrite Equation (S1) in 2D, we have

$$H[\psi] = \int_S \{\frac{1}{2}|W\nabla\psi|^2 + f[\psi(\overrightarrow{x})]\}d^2x = \int_S L[\psi, \nabla\psi]d^2x. \tag{S2}$$

The phase field evolution obeys a dissipative Allen-Cahn equation:

$$\frac{\partial\psi}{\partial t} = -K\frac{\delta H}{\delta\psi}, \tag{S3}$$

in which the variation derivative will be written as

$$\frac{\partial\psi}{\partial t} = -K\frac{\delta H}{\delta\psi} = -K\{\frac{\partial L}{\partial\psi} - \nabla\frac{\partial L}{\partial\nabla\psi}\} = -K(\frac{\partial f}{\partial\psi} - W^2\nabla^2\psi). \tag{S4}$$

Taking a characteristic time constant of adatom attachment $\tau_\psi = 1/K$, we have

$$\tau_\psi\frac{\partial\psi}{\partial t} = W^2\nabla^2\psi - \frac{\partial f}{\partial\psi}, \tag{S5}$$

where $f$ denotes the bulk contribution of the free energy density.

Traditionally, $f$ takes the form of a double-well potential, with two local minima corresponding to the two phases in transition. This potential is suitable to simulate a monolayer growth, with $\psi = 0$ being the precursor phase, $\psi = 1$ the deposited film phase, and a smooth transition between 0 and 1 as the interface.[5] To simulate multilayer growth, the order parameter $\psi$ is selected such that $\psi/2$ represents the height of the epilayer surface, and $\psi_s/2$ is the height of the surface of the substrate (or the underlying layer), in units of monolayer thickness. Thus, when $f$ takes the general functional form of $A\cos[\pi(\psi - \psi_s) + B] + C\psi$, it satisfies the criteria below:

(1) $f$ has multiple equally spaced local minima, each of which occurs when the deposited film height ($(\psi - \psi_s)/2$) increases by one full monolayer. In other words, the neighboring local minima of $f$ with respect to $\psi$ have equal distances of $\Delta\psi = 2$;

(2) The free energy changes as the deposited film increases in thickness. The constant $C$ has the physical significance of the free energy difference between the deposited film and the precursor. Under deposition conditions, in which the film phase has lower free energy than that of the precursors, and deposition happen spontaneously, the free energy should decrease, thus $C < 0$.

The oversaturation of the precursor ($u$) contributes to $f$ in two parts. First, it shifts the local minima of $f$ with respect to $\psi$, such that at a higher oversaturation, the system has higher momentum for the film to grow thicker. Thus mathematically, $u$ contributes to the phase shift parameter $B$. $u$ also contributes to the free energy difference $C$, as the degree of oversaturation of the precursor influences the free energy of the precursor phase, hence the free energy difference between the two phases. Without loss of generality, the coefficient $A$ reflects the strength of the potential, which is independent to $\psi$, when considering the limit of small supersaturations.[4] Karma and Plapp proposed that a free energy density of

$$f(\psi) = \frac{\sqrt{1+\lambda^2 u^2}}{\pi}\cos[\pi(\psi - \psi_s) + \sin^{-1}\frac{\lambda u}{\sqrt{1+\lambda^2 u^2}}] - \lambda u\psi \tag{S6}$$

can well reflect the contribution of the supersaturation of the precursor within the functional discussed above.

Inserting Equation (S6) into (S5), we have

$$\tau_\psi \frac{\partial H}{\partial t} = -\frac{\partial H}{\partial \psi} = W^2\nabla^2\psi + \sin[\pi(\psi-\psi_s)] + \lambda u\{1+\cos[\pi(\psi-\psi_s)]\}, \tag{S7}$$

which is the governing equation of the phase field model of this work.[2]

## Anisotropy of the interface energy

The term $W^2\nabla^2\psi$ derived from

$$-\frac{\delta\frac{1}{2}|W\nabla\psi|^2}{\delta\psi} = \nabla\frac{\partial\frac{1}{2}|W\nabla\psi|^2}{\partial\nabla\psi} = W^2\nabla^2\psi, \tag{S8}$$

assumes an isotropic and hence constant $W$. However, in this work, the interface width $W$ takes the form of

$$W(\theta) = W_0\{1+\delta[1+\cos(\nu\theta)]\}, \quad \theta = atan2(\frac{\partial\psi}{\partial y}, \frac{\partial\psi}{\partial x}), \tag{S9}$$

to simulate the growth of the trigonal domains of the TMDs. In this case, the variation derivative in Equation (S8) becomes:[6]

$$\begin{aligned}
&-\frac{\delta\frac{1}{2}|W(\theta)\nabla\psi|^2}{\delta\psi} \\
=&\nabla\frac{\partial\frac{1}{2}|W(\theta)\nabla\psi|^2}{\partial\nabla\psi} \\
=&W(\theta)^2\nabla^2\psi + 2W(\theta)\frac{dW(\theta)}{d\theta}|\nabla\psi|\hat{\mathbf{z}}\cdot\nabla\times\frac{\nabla\psi}{|\nabla\psi|} + \{[\frac{dW(\theta)}{d\theta}]^2 + W(\theta)\frac{d^2W(\theta)}{d\theta^2}\}|\nabla\psi|\nabla\times\frac{\nabla\psi}{|\nabla\psi|}.
\end{aligned} \tag{S10}$$

Equation (S6) ensures that the minima of $f$ fall at a fixed value in the vicinity of $\psi-\psi_s = 2n+1$, in which $n$ is integer. In this sense, the integer $n$ can be used to record the layer number of the deposited multilayer film. In order to simulate the AB stacking growth driven by a two-layer-deep

screw dislocation, Equation (S9) can be changed to

$$W(\theta) = \begin{cases} W_0\{1+\delta[1+\cos(\nu\theta)]\}, & n \text{ is odd} \\ W_0\{1+\delta[1+\cos(\nu\theta+\pi)]\}, & n \text{ is even} \end{cases} \tag{S11}$$

## The coupling constant $\lambda$

Following previous works,[2,5,7] the parameters in Equation (S7) take the unit time scale of $\tau_\psi$ and the length scale $W_0$, and become non-dimensionalized. Without the loss of generality, the system can always rescale to make the coupling coefficient $\lambda$ and the diffusion coefficient of the precursor $D$ the only two independent variables. $\lambda$ connects the phase field $\psi$ with the precursor supersaturation field $u$. For the physical significance of $\lambda$, *vide infra*.

The phase field model itself merely provides a numerical framework that can provide phenomenological description of the film growth. In order for the model to have physical significance, it has to be correlated to the sharp interface model:

$$\begin{aligned} \frac{\partial u}{\partial t} &= D\nabla^2 u - \frac{u}{\tau_s} + F - \frac{1}{2}\frac{\partial \psi}{\partial t}, \\ v_n &= D[(\frac{\partial u}{\partial n})_+ - \frac{\partial u}{\partial n})_-], \\ u &= d_0\kappa, \end{aligned} \tag{S12}$$

where $v_n$ is the interface normal velocity, $(\partial u/\partial n)_{+/-}$ is the normal concentration gradient on the lower (+) and upper (-) side of the step, and $\kappa$ is the curvature of the interface. Karma *et al.* have demonstrated that under the thin-interface limit, the phase-field equations can be written as[2,3,8]

$$\begin{aligned} \frac{\partial u}{\partial t} &= D\nabla^2 u - \frac{u}{\tau_s} + F - \frac{1}{2}\frac{\partial \psi}{\partial t}, \\ v_n &= D[(\frac{\partial u}{\partial n})_+ - \frac{\partial u}{\partial n})_-], \\ u &= d_0\kappa + a_1(\frac{\tau_\psi}{\lambda W} - \frac{a_2 W}{D})v_n, \end{aligned} \tag{S13}$$

In order for the $v_n$ term to disappear in the third equation to correspond to the sharp-interface model in Equation (S12), $\lambda$ should be chosen as $\lambda = \tau_\psi D/a_2 W$, thus losing its independence. In the same reference, it has been calculated that $a_2 = 0.510442$, and the parameters are chosen as listed in Table 1 in the main text.

## Selection of a single precursor in the model

There has been significant debate whether the locale of the reaction is in the gas phase or on the substrate. Many studies have proposed that, especially in a CVD process, the chalcogenides have formed in the gas phase before their deposition onto the substrate.[9] In this sense, because the phase transformation described in the model of this work is the transition between solid and the ad-molecule "gas" phase, using one field for the precursor realistically captures the formation mechanism of the experimental condition.

In many synthesis methods such as MOCVD and MBE, separate precursors do assemble themselves after adsorption onto the surface, and the chalcogen-metal ratio is an important factor that influences the growth. Specifically, the chalcogen-metal ratio mainly affects the growth at the atomic level, such as the film continuity,[10] the relative stability of flake edges,[7,11] and the chemical constituents of the flake and homogeneous nuclei,[9,12] *etc.* A continuum method such as the phase-field model is not suitable to describe these atomistic properties. Instead, supplementary first-principles calculations are required. These topics have been covered in detail in our previous work.[10,12]

Meanwhile, for a quantitative comparison or prediction, a phase-field method can include more details based on the selection of precursors and the specific reactions involved. However, this work aims at finding the generic growth patterns after defect based heterogeneous nucleations, therefore, too many additional details may begin to derail from the theme of this work. Similar methods have proved effective to use a single precursor to describe the growth behavior of layered chalcogenides in a generalized perspective.[7,13]

## The uniformity of the diffusion coefficient

Anisotropic diffusion will play a role in the growth morphology. Meca *et al.* conducted a comprehensive study focused on this factor.[5,14] Although these works were done on graphene, many of the conclusions in their work are transferrable to the model in this work. Generally speaking, the anisotropy of the diffusion of the precursor and the anisotropy of the domain itself (edge energy, reaction kinetics, *etc.*) work cooperatively in the determination of the shape of the domain.

In this work, an isotropic diffusion across the substrate is assumed. In many cases, where chalcogenides with trigonal symmetry are deposited onto substrates with hexagonal symmetry, such as highly oriented pyrolytic graphite, the trigonal domain will align with the hexagonal substrate. As a result, the precursors have facile diffusion paths towards the six stable and metastable edges, and the diffusivity can be treated as isotropic for a good approximation. Even when the substrate itself has three-fold symmetry, such as sapphire and the TMD itself, the diffusion of the precursors on the first atomic layer of these substrates is not affected significantly, and still behaves with a six-fold diffusion symmetry.

Even if the substrate has diffusion anisotropy that is inconsistent with the symmetry of the deposited flake, it is noteworthy that from the second layer on, the film growth is in fact autoepitaxy, *i.e.*, the growth of the same material on itself. According to the discussions above, from the second layer on, it is suitable to select an isotropic diffusion coefficient.

As a confirmation of these assumptions, simulations with a non-uniform diffusion coefficient $D$ are performed. Two types of anistropy of the diffusion coefficient, namely the 4-fold and the 6-fold anisotropy, are selected. For each symmetry, 2 cases are studied (Figure S1). The simulation results show that in the early stage, the domain shape shows a combined influence of the substrate anisotropy and the structural anisotropy. As the domain grows in size, the influence of the diffusion anisotropy diminishes, because the diffusion of the precursors on the film can compensate the insufficient precursor from the substrate.

It is noteworthy that with a changing diffusion coefficient, in every integration iteration, the matrix of the governing diffusion equation Eqation (2) in the main text will be refreshed, and

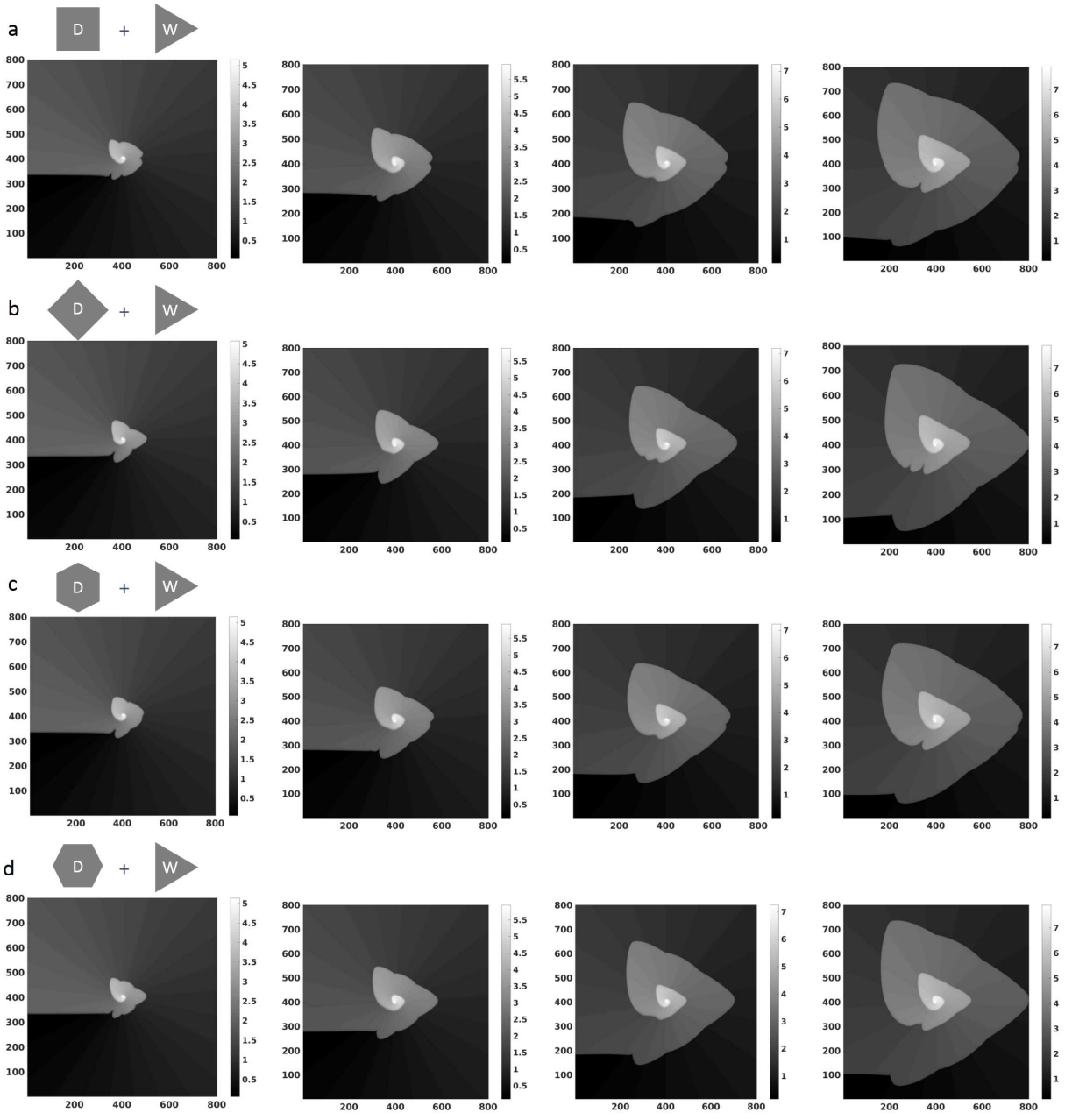


Figure S1: The simulation result of the growth on substrates with different diffusion anisotropy. The initial screw dislocation is the same as Figure 2a in the main text. The simulation shows that the diffusion anisotropy has an influence on the first layer in the initial stages. However, as the domain grows in size, due to the on-flake diffusion, the influence of the anisotropy of $D$ becomes less significant. Moreover, from the second layer on, the growth morphology will not be affected by a non-uniform $D$ on the substrate.

factorized, which is a computationally expensive process. Since the anisotropy of $D$ does not play a significant role after reaching the steady state, it is a reasonable approximation to consider an isotropic and uniform $D$.

## The dependence of spiral frequency on flux

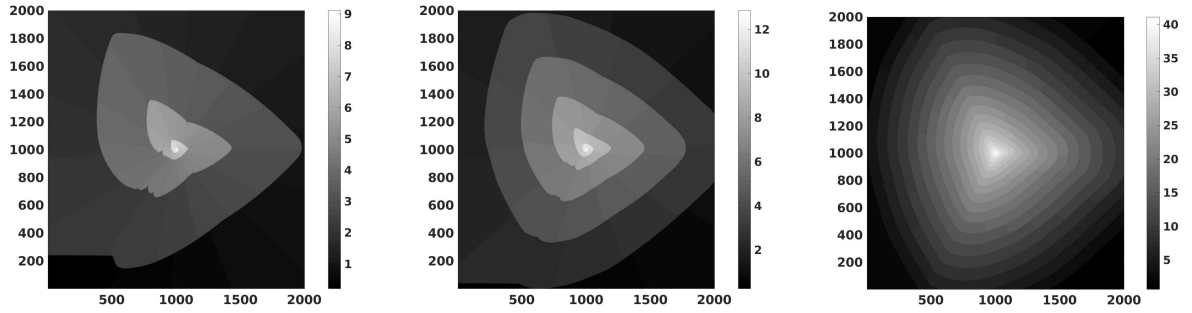


(a) (b) (c)

Figure S2: Phase-field simulation results of growths driven by a single spiral, under increasing flux (left to right: $F$=0.05, 0.1, 1).

Figure S2 shows the phase-field simulation results under different flux, with other parameters unchanged. With similar area, the width of the step edge decreases with increasing flux. This is in agreement with both the previous phase-field calculations and analytical models.[3,15]

## Extended discussion on the obtaining of hexagonal islands

For the epitaxy on an isotropic substrate, the anisotropy of the film is determined by two factors: the inequity on the structural stability of different edges (tuned by the anisotropy of $W$ in Equation (2) in the main text), and the inequity on reactivity of the respective edges (tuned by the anisotropy of $\tau_\psi$), both of which depend on the chemical potentials of the precursors. The monolayers of a 2H crystal, for example, $WSe_2$, have a structure with trigonal symmetry. Under common conditions, the edges with higher energy are simultaneously the ones with higher reactivity, therefore they

quickly diminish during the growth, making the domain trigonal. For this type of crystal, there are two scenarios to obtain hexagonal domains with parallel spiral lines:

(1) both the reactivity and energy of the two sets of edges are comparable. In order to establish this condition in the phase field model, the rotational anisotropy $\nu$ takes the value of 6 (instead of 3 in the main text). $\tau_\psi$ either conforms with $W$, taking rotation order of 6 and align with $W$, or is uniform across the polar angle, as it is throughout the main text.

(2) the energy of the two sets of edges are not equal, but the edges with lower energy are tuned by the precursor environment to have higher reactivity. In the phase field model, this condition means that $W$ takes the rotation order of 3, as it is in the main text, but $\tau_\psi$ also takes an isotropic form as:

$$\tau_\psi(\theta) = \tau_{\psi 0}\{1 + \delta_\psi[1 + \cos(\nu_\psi \theta_\psi)]\}, \quad \theta_\psi = atan2(\frac{\partial \psi}{\partial y}, \frac{\partial \psi}{\partial x}) + \varphi_\psi, \tag{S14}$$

and $\varphi_\psi$ takes the value of $\pi$ so that it is 180° rotation with respect to the anisotropy of $W$.

Both these conditions will result in the hexagonal domains (Figure S3), but they are in fact driven by different mechanisms. As these discussions are based on the comparison of edges only, these conclusions are transferrable to the growth initiated by other nucleation mechanisms beside screw dislocations.

# Additional characterization of molecular beam epitaxy (MBE) grown $Bi_2Se_3$

A bulk $Bi_2Se_3$ crystal, grown by chemical vapor transport (CVT), was purchased from HQ graphene and concurrently characterized along with the MBE-grown samples for crystallographic confirmation. Figure S4 shows the Raman shifts for both the MBE-grown and CVT reference samples, where the $E^2_{1g}$ and $A^2_{1g}$ peaks are clearly visible and overlap closely. Figure S5 shows out-of-plane XRD data for the MBE sample grown on sapphire. The dominant (006) peak position is consis-

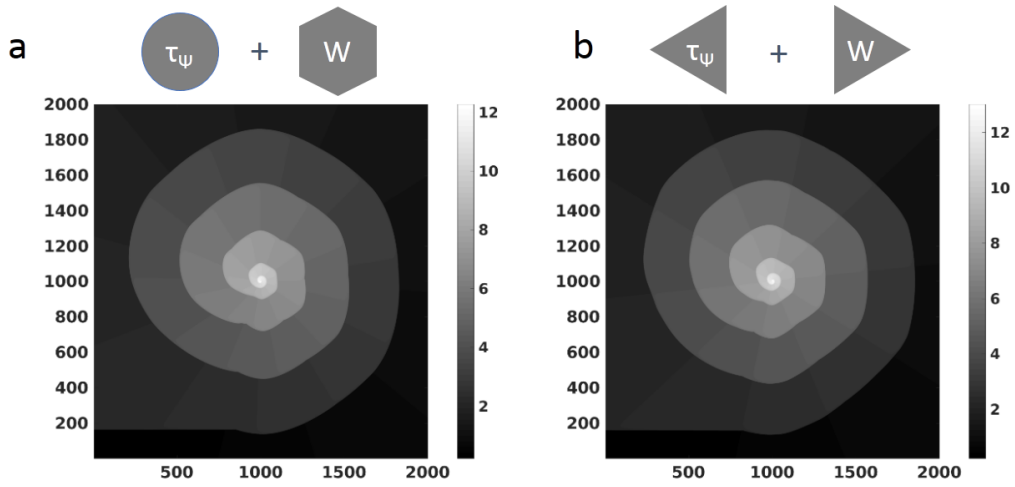


Figure S3: Driven by the same nucleation (Figure 2a in the main text), under normal conditions, the domain assumes trigonal symmetry (Figure S1b). However, if either of the conditions described in this section is satisfied, a hexagonal domain will be obtained due to either equalized edge energy (a), or the common result by the respective thermodynamic stability and kinetic inertia (b).

tent with theoretical predictions for quintuple-layered $Bi_2Se_3$. Furthermore, the FWHM of 0.239 indicate a high degree of crystallinity in the MBE-grown film. During deposition, the MBE-grown film was monitored by *in-situ* reflection high-energy electron diffraction (RHEED). The images seen in Figure S6 show the diffraction patterns along the $[10\bar{1}0]$ and $[11\bar{2}0]$ azimuthal directions. The ability to independently observe the different diffraction patterns at their corresponding azimuthal angles indicates rotational alignment with the single-crystal c-plane sapphire substrate. Furthermore, the sharpness of the RHEED streaks indicates an exceptionally flat top surface. Figure fig:XPS shows the XPS scans of the Bi 4f and Se 3d core levels of the MBE-grown film. The sample was exposed to atmospheric conditions for 15 minutes prior to loading into the XPS system, but still shows no sign of oxidation. Figure S8 shows a cross-sectional scanning transmission electron microscopy (STEM) image of the MBE-grown $Bi_2Se_3$. The film clearly exhibits a high degree of flatness, the quintuple-layer structure, uniformity, and is absent of visible defects.

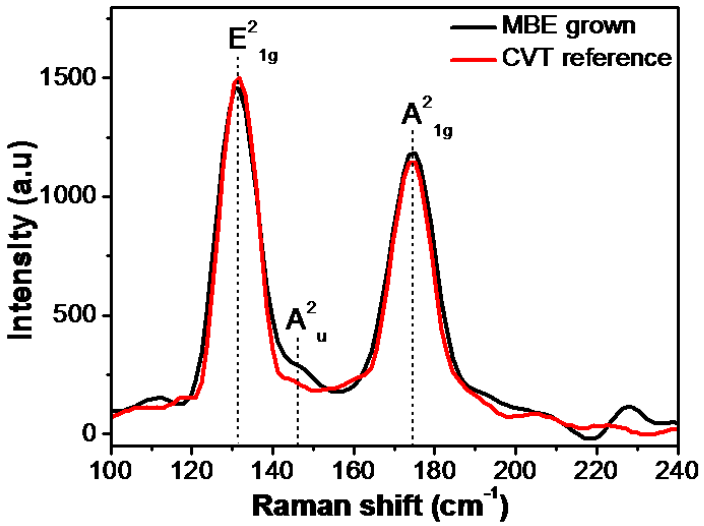


Figure S4: Raman spectra of chemical vapor transport (CVT) and MBE-grown $Bi_2Se_3$ films showing overlapping peak positions.

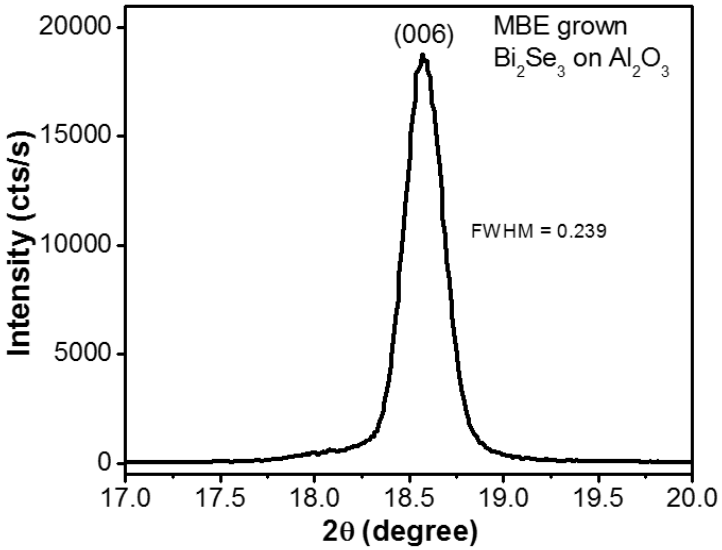


Figure S5: X-ray diffraction (XRD) scan showing a sharp peak at the expected angle for the (006) diffraction plane.

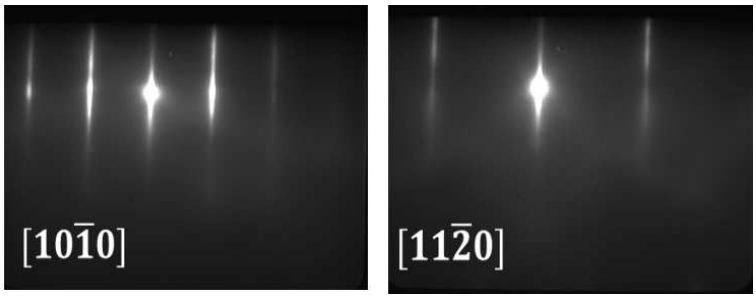


Figure S6: Reflection high energy electron diffraction (RHEED) patterns along the $[10\bar{1}0]$ and $[11\bar{2}0]$ azimuthal directions.

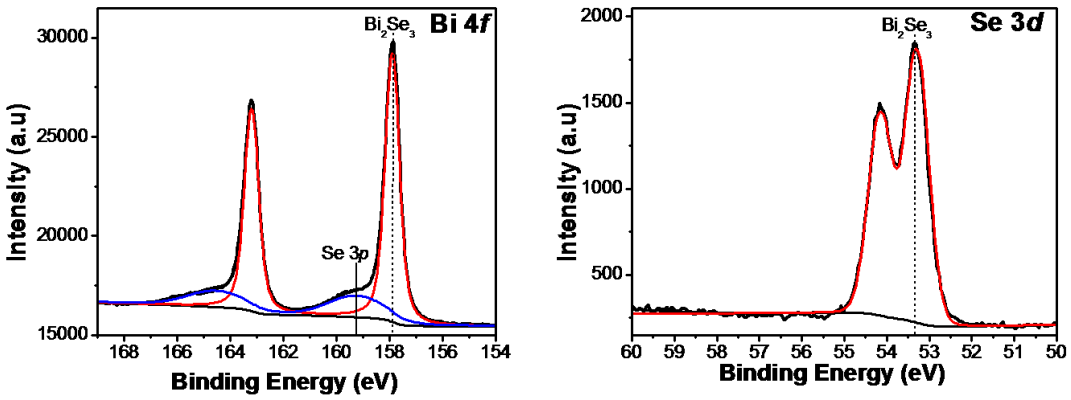


(a) (b)

Figure S7: X-ray photoelectron spectroscopy (XPS) spectra of the Bi 4f and Se 3d core levels of $Bi_2Se_3$ grown on c-plane sapphire.

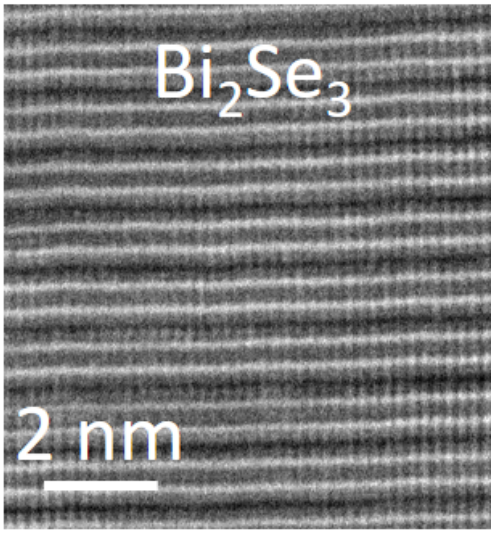


Figure S8: Cross-sectional transmission electron microscopy (TEM) of the MBE-grown $Bi_2Se_3$ on c-plane sapphire.

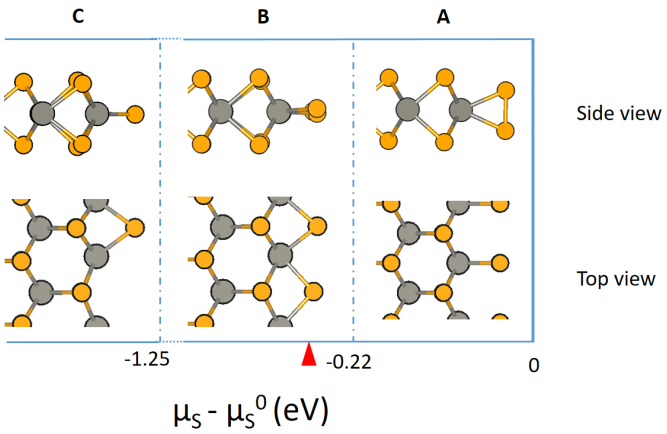


▲ denotes $\mu_S - \mu_S^0$ = -0.34 eV at 800 K, 0.1 MPa sulfur vapor pressure (http://kinetics.nist.gov). $\mu_S^0$ is the chemical potential of sulfur bulk at 0 K.

A is the fully sulfurized Mo zigzag edge, B is half-sulfurized and C is quarter-sulfurized. The following reaction is considered to determine the edge morphology at different chemical potential of sulfur vapor.
$A \rightarrow B + S$, $\Delta G_1 = E_B + \mu_S - E_A$ ; $B \rightarrow C + S$, $\Delta G_2 = E_C + \mu_S - E_B$

(a)

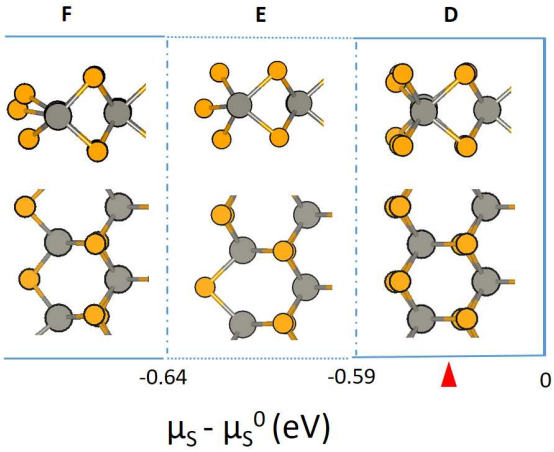


▲ denotes $\mu_S - \mu_S^0$ = -0.34 eV at 800 K, 0.1 MPa sulfur vapor pressure (http://kinetics.nist.gov).

(b)

Figure S9: The change in the edge configuration of the isolated $MoS_2$ with respect to the chemical potential of sulfur vapor. Left is the metal zigzag edge, and right is the sulfur zigzag edge. The red triangle denotes the chemical potential of sulfur at 800K and 0.1 MPa. Under this condition, the sulfur zigzag edge is fully chalcogenized, but the Mo zigzag edge is only half-chalcogenized. However, when a substrate is present, the fully chalcogenized Mo zigzag edge will be stabilized by 0.31 eV.[16,17] In this sense, both metal and chalcogen zigzag edges are fully sulfurized by considering the substrate effect.

# Additional theoretical mechanism analysis

The case of $MoS_2$ is taken as an example to investigate the comparison of the stabilities and growth rates of different edges. The degree of chalcogenization at the domain edge of $MoS_2$ is a function of the chemical potential of the precursors. Due to the much lower partial pressure of Mo precursor vapor (*e.g.* $MoO_3$) compared with that of S vapor in a typical S rich synthesis condition, the change on the chemical potential of S will determine the edge morphology, as discussed in the following. Figure S9 shows the edge evolution with respect to the chemical potential of sulfur, in which A-C are the metal zigzag edges, and D-F are the chalcogen zigzag edges. A and D are fully sulfurized edges, E is three-quarter-sulfurized, B and F are half-sulfurized, and C is quarter-sulfurized. The following reaction is considered to determine the edge morphology at different chemical potential of sulfur vapor:

$$(A) \rightarrow (B) + 2S, \quad \Delta G_1 = E_B + 2\mu_S - E_A, \tag{S15}$$

$$(B) \rightarrow (C) + S, \quad \Delta G_2 = E_C + \mu_S - E_B, \tag{S16}$$

$$(D) \rightarrow (E) + S, \Delta G_3 = E_E + \mu_S - E_D, \tag{S17}$$

$$(E) \rightarrow (F) + S, \Delta G_4 = E_F + \mu_S - E_E. \tag{S18}$$

The chemical potential of sulfur vapor is calculated by

$$\begin{aligned} \mu_S(T,p) - \mu_S(T=0K,p_0) &= [\mu_S(T,p) - \mu_S(T,p_0)] + [\mu_S(T,p_0) - \mu_S(T=0K,p_0)] \\ &= k_B T \ln(\frac{p}{p_0}) + [\Delta h_S(T,p_0) - T\Delta S_S(T,p_0)], \end{aligned} \tag{S19}$$

where $\Delta h_S(T,p_0) = h_S(T,p_0) - h_S(T=0K,p_0)$, $\Delta S_S(T,p_0) = S_S(T,p_0) - S_S(T=0K,p_0)$, and $p_0 = 0.1MPa$. $\Delta h_S(T,p_0)$, $\Delta S_S(T,p_0)$ can be found in standard standard thermodynamic tables (http://kinetics.nist.gov). $\mu_S(T=0K,p_0)$ is the chemical potential $\mu_S^0$ of sulfur bulk calculated through DFT at $T=0K$.

Under a given set of growth conditions, for example in Figure S9, 800 K and 0.1MPa, the

chalcogen zigzag edge is more easily fully chalcogenized than the metal zigzag edge. However, in the presence of a substrate, both Mo and S zigzag edges are fully chalcogenized, therefore the climb-up phenomenon will be observed in this condition.[16,17]

The edge growth energy barriers are calculated through a sequential reaction scheme, by considering the growth process as sequentially adding gas phase $MoS_2$ units. This is based on the fact that Mo precursor vapor will react with S vapor in the gas phase forming the $MoS_2$ fragment,[9] then deposit on the substrate. The growth barriers arise from the fact that the most stable adsorption site of a $MoS_2$ fragment is different from the lattice site before the edge is fully covered by $MoS_2$ fragments. In order for the edge to grow conformally after full coverage, these distorted $MoS_2$ fragments need to be activated back to the lattice sites, which yields transition states and barriers as demonstrated in Figure S10. The difference of 0.33 eV on the activation energy makes the growth rate of the metal zigzag edge much slower than that of the chalcogen zigzag edge in the sulfur rich synthesis condition ($\exp(0.33eV/kT) = 120$).

These barrier calculations also show that when the $MoS_2$ fragment is directly attached onto the domain edges, the thermodynamically unstable edge also has the lower barrier. Therefore, in normal conditions, $MoS_2$ flakes have the shape of a triangle. If through this mechanism the domain assumes the shape of a hexagon, it is a result of a fine tuning of the chemical potential of the precursors, so that the two sets of edges have the comparable stabilities and growth rates.[11,18]

## The mechanistic analysis of the formation of Frank-Read source for 1T-TMDs and $Bi_2Se_3$

First of all, similar to $MoS_2$, both $ZrS_2$ and $Bi_2Se_3$ prefer metal vacancies to align linearly than distributing sparsely (Figure S11a,b). However, different from $MoS_2$, due to the existence of inversion symmetry within the monolayer, the dimerization tendency of dangling chalcogen atoms is resolved between the two adjacent edges (Figure S12 for $ZrS_2$, and Figure S13 for $Bi_2Se_3$). The inter-edge dimerization naturally causes edge lift-up and generate a line of chalcogen dangling

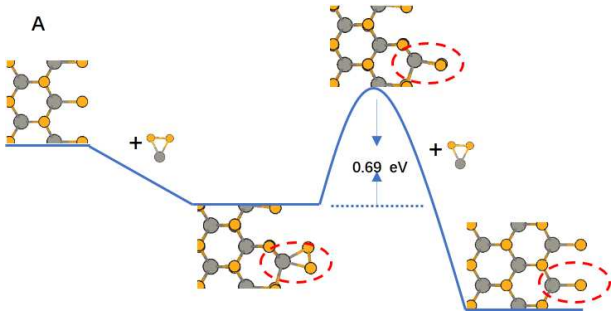


(a)

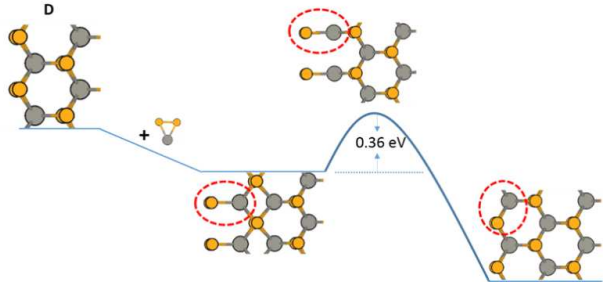


(b)

Figure S10: The proposed attachment mechanism. The newly attached group is circled. For both the metal zigzag edge and the chalcogen zigzag edge, an energy barrier exists to reconfigure the structure from a stable adsorption site to the lattice site.

bonds. When the line of dangling bonds is ended on both side, it will form the Frank-Read core similar to 2H-TMDs.

# Kinetic Monte Carlo simulation of the evolution of an in-flake void during deposition

The KMC simulation follows the method described in the reference[19] with the parameters calculated via first-principles in our previous work.[10] The simulations start from a circular void (Figure S14a), and are performed under chalcogen-rich conditions, with a flux of 1 ML/s and a chalcogen-metal ratio of 200. The substrate temperature is set at 773 K.

Figure S14 shows the starting configuration and several simulation results. Three types of defect configurations are observed. Simple voids (Figure S14b) do not contribute to the multilayer growth mechanism discussed in the manuscript, therefore they are dropped from further discus-

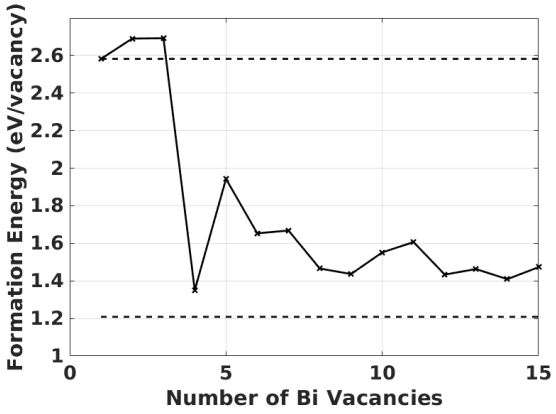


(a)


(b)

Figure S11: Change of formation energy of linearly arranged metal vacancies in monolayer $ZrS_2$ (a) and $Bi_2Se_3$ (b) with respect to the linear length. The formation energies of individual sparse metal vacancies and infinitely long metal vacancy line are marked by the dashed line on top and bottom, respectively.

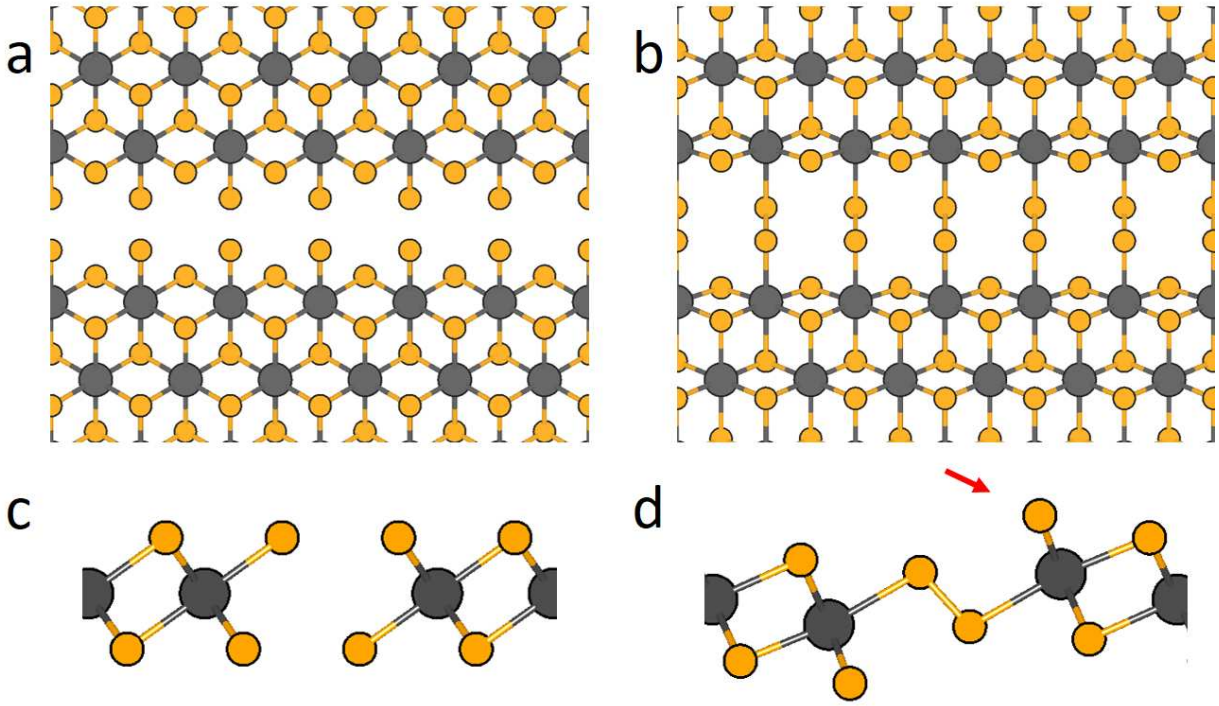


Figure S12: The top view (a,b) and side view (c,d) of $ZrS_2$ with linearly arranged metal vacancies, before (a,c) and after (b,d) structural optimization through chalcogen dimerization across the vacancy line. Metal atoms (Zr) are represented by gray orbs, and chalcogen atoms (S) by yellow orbs. Lift-up of one edge is observed after chalcogen dimerization (d), with a line of dangling bonds exposed (red arrow) as nucleation site.

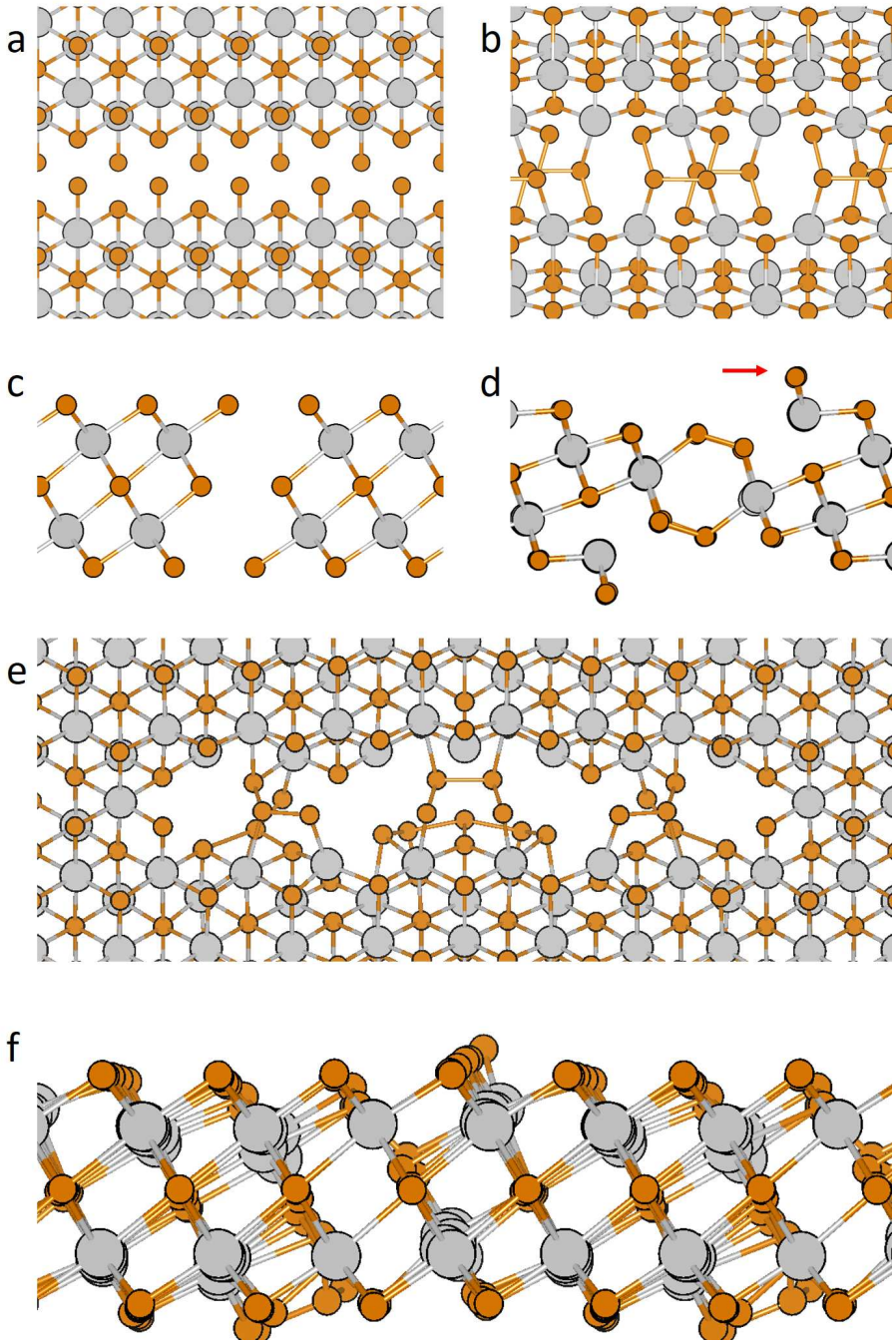


Figure S13: The top view (a,b) and side view (c,d) of $Bi_2Se_3$ with linearly arranged metal vacancies, before (a,c) and after (b,d) structural optimization through chalcogen dimerization across the vacancy line. Metal atoms (Bi) are represented by gray orbs, and chalcogen atoms (Se) by yellow orbs. Lift-up of one edge is observed after chalcogen dimerization (d), with a line of dangling bonds exposed (red arrow) as nucleation site. When the metal vacancy line is terminated at the ends, the lift-up in the middle of the line will form a Frank-Read core (e,f).

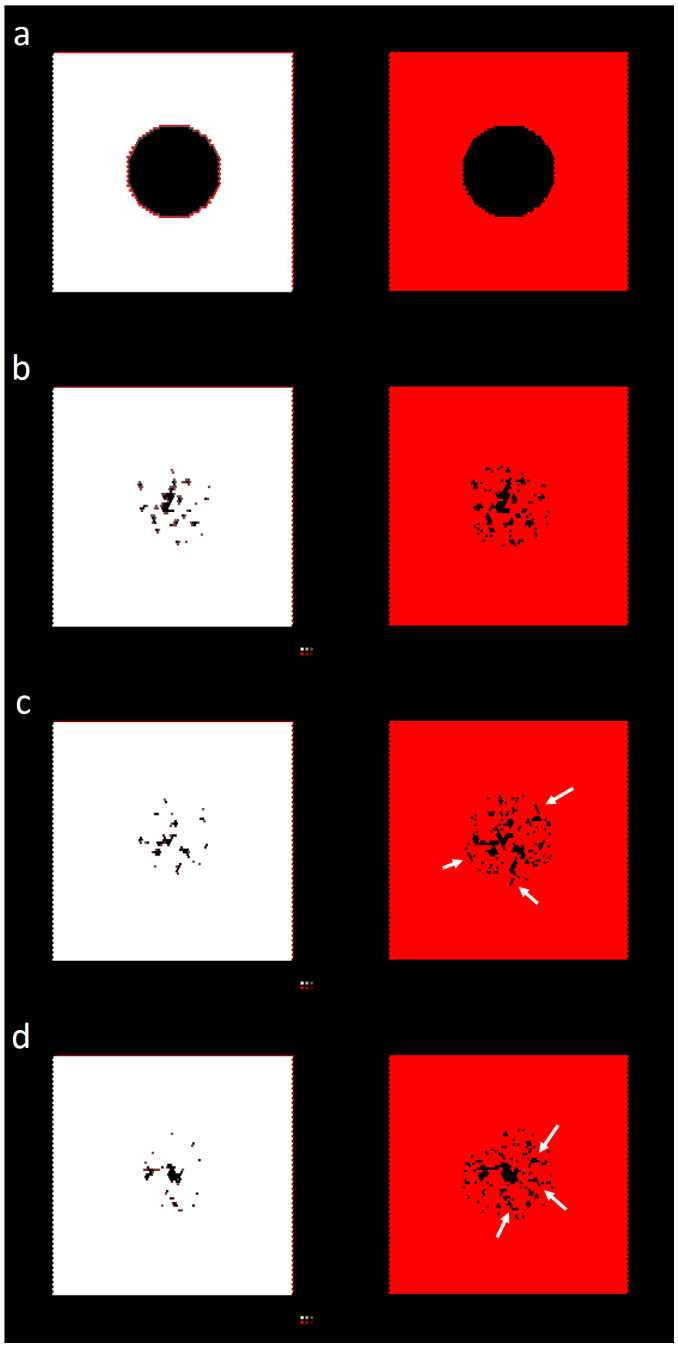


Figure S14: The kinetic Monte Carlo simulation of the evolution of an in-flake void. The left panel shows the top view of the sandwiched structure, with the pixel color coded to represent metal (red) and chalcogen (white/grey) atoms. To show the metal vacancies underneath the chalcogen layer, the middle layer is isolated and visualized in the right panel. (a) the initial structures of an in-flake void. (b) the formation of voids after deposition. (c) the formation of linearly aligned metal vacancies (arrowed). (d) metal vacancies forming 120-degree broken lines (arrowed).

sions. Linearly aligned vacancies can be naturally formed from the diminishing of a void (arrowed in Figure S14c). In addition, linearly aligned vacancies can join and form a broken line of vacancies, with two ends and a vertex. Due to the atomic configuration of the TMDs, the broken lines are often oriented 120° (arrows in Figure S14d). The chalcogen dimerization induced strain also applies to the broken lines: in-line dimerization at the two ends exerts compressive strain along the broken line, and out-of-line dimerization away from the ends and at the vertex exerts tensile strain perpendicular to the lines. The unbalanced strain, under kinetic perturbation, can cause the climb-up of one edge over the other, forming a new Frank-Read source.

# References


1. Hohenberg, P. C.; Halperin, B. I. Theory of Dynamic Critical Phenomena. *Rev. Mod. Phys.* **1977**, *49*, 435–479.

2. Karma, A.; Plapp, M. Spiral Surface Growth without Desorption. *Phys. Rev. Lett.* **1998**, *81*, 4444.

3. Karma, A.; Rappel, W.-J. Quantitative Phase-field Modeling of Dendritic Growth in Two and Three Dimensions. *Phys. Rev. E* **1998**, *57*, 4323–4349.

4. Liu, F.; Metiu, H. Stability and Kinetics of Step Motion on Crystal Surfaces. *Phys. Rev. E* **1994**, *49*, 2601.

5. Meca, E.; Lowengrub, J.; Kim, H.; Mattevi, C.; Shenoy, V. B. Epitaxial Graphene Growth and Shape Dynamics on Copper: Phase-field Modeling and Experiments. *Nano Lett.* **2013**, *13*, 5692–5697.

6. McFadden, G. B.; Wheeler, A. A.; Braun, R. J.; Coriell, S. R.; Sekerka, R. F. Phase-field Models for Anisotropic Interfaces. *Phys. Rev. E* **1993**, *48*, 2016–2024.

7. Wu, J.; Hu, Z.; Jin, Z.; Lei, S.; Guo, H.; Chatterjee, K.; Zhang, J.; Yang, Y.; Li, B.; Liu, Y. *et al.* Spiral Growth of $SnSe_2$ Crystals by Chemical Vapor Deposition. *Adv. Mater. Interfaces* **2016**, *3*, 1 – 8.

8. Caginalp, G. Stefan and Hele-Shaw Type Models as Asymptotic Limits of the Phase-field Equations. *Phys. Rev. A* **1989**, *39*, 5887.

9. Li, H.; Li, Y.; Aljarb, A.; Shi, Y.; Li, L.-J. Epitaxial Growth of Two-Dimensional Layered Transition-Metal Dichalcogenides: Growth Mechanism, Controllability, and Scalability. *Chem. Rev. ASAP* **2017**, *0*, null, PMID: 28682055.

10. Nie, Y.; Liang, C.; Zhang, K.; Zhao, R.; Eichfeld, S. M.; Cha, P.-R.; Colombo, L.; Robinson, J. A.; Wallace, R. M.; Cho, K. First Principles Kinetic Monte Carlo Study on the Growth Patterns of $WSe_2$ Monolayer. *2D Mater.* **2016**, *3*, 025029.

11. Govind Rajan, A.; Warner, J. H.; Blankschtein, D.; Strano, M. S. Generalized Mechanistic Model for the Chemical Vapor Deposition of 2D Transition Metal Dichalcogenide Monolayers. *ACS Nano* **2016**, *10*, 4330–4344, PMID: 26937889.

12. Yue, R.; Nie, Y.; Walsh, L. A.; Addou, R.; Liang, C.; Lu, N.; Barton, A. T.; Zhu, H.; Che, Z.; Barrera, D. *et al.* Nucleation and Growth of WSe2: Enabling Large Grain Transition Metal Dichalcogenides. *2D Mater.* **2017**, *4*, 045019.

13. Artyukhov, V. I.; Hu, Z.; Zhang, Z.; Yakobson, B. I. Topochemistry of Bowtie- and Star-Shaped Metal Dichalcogenide Nanoisland Formation. *Nano Lett.* **2016**, *16*, 3696–3702, PMID: 27187078.

14. Meca, E.; Shenoy, V. B.; Lowengrub, J. Phase-field Modeling of Two-dimensional Crystal Growth with Anisotropic Diffusion. *Phys. Rev. E* **2013**, *88*, 052409.

15. Zhuang, A.; Li, J.-J.; Wang, Y.-C.; Wen, X.; Lin, Y.; Xiang, B.; Wang, X.; Zeng, J. Screw-

Dislocation-Driven Bidirectional Spiral Growth of Bi2Se3 Nanoplates. *Angew. Chem. Int. Ed.* **2014**, *53*, 6425–6429.

16. Bollinger, M.; Jacobsen, K. W.; Nørskov, J. K. Atomic and Electronic Structure of $MoS_2$ Nanoparticles. *Phys. Rev. B* **2003**, *67*, 085410.

17. Lauritsen, J. V.; Kibsgaard, J.; Helveg, S.; Topsøe, H.; Clausen, B. S.; Lægsgaard, E.; Besenbacher, F. Size-dependent Structure of $MoS_2$ Nanocrystals. *Nature Nanotechnol.* **2007**, *2*, 53–58.

18. Wang, S.; Rong, Y.; Fan, Y.; Pacios, M.; Bhaskaran, H.; He, K.; Warner, J. H. Shape Evolution of Monolayer $MoS_2$ Crystals Grown by Chemical Vapor Deposition. *Chem. Mater.* **2014**, *26*, 6371–6379.

19. Nie, Y.; Liang, C.; Cha, P.-R.; Colombo, L.; Wallace, R. M.; Cho, K. A Kinetic Monte Carlo Simulation Method of van der Waals Epitaxy for Atomistic Nucleation-growth Processes of Transition Metal Dichalcogenides. *Sci. Rep.* **2017**, *7*, 1 – 13.